

Physics-Informed Graph Learning for Robust Fault Location in Distribution Systems

Wenting Li, *Member, IEEE*, Deepjyoti Deka, *Senior Member, IEEE*,

Abstract—The rapid growth of distributed energy resources potentially increases power grid instability. One promising strategy is to employ data in power grids to efficiently respond to abnormal events (e.g., faults) by detection and location. Unfortunately, most existing works lack physical interpretation and are vulnerable to the practical challenges: sparse observation, insufficient labeled datasets, and stochastic environment. We propose a physics-informed graph learning framework of two stages to handle these challenges when locating faults. Stage-I focuses on informing a graph neural network (GNN) with the geometrical structure of power grids; stage-II employs the physical similarity of labeled and unlabeled data samples to improve the location accuracy. We provide a random walk-based underpinning of designing our GNNs to address the challenge of sparse observation and augment the correct prediction probability. We compare our approach with three baselines in the IEEE 123-node benchmark system, showing that the proposed method outperforms the others by significant margins, especially when label rates are low. Also, we validate the robustness of our algorithms to out-of-distribution-data (OOD) due to topology changes and load variations. Additionally, we adapt our graph learning framework to the IEEE 37-node test feeder and show high location performance with the proposed training strategy.

Index Terms—Graph neural networks, fault location, distribution systems, low label rates, physics-informed machine learning, OpenDSS

I. INTRODUCTION

Renewable energies, such as solar and wind power, can meet the ever-increasing electricity demand without further accelerating climate changes. However, the expansion of random, intermittent distributed energy resources (DERs) in distribution grids has potentially increased instability. Current power systems have not successfully adapted to the distinctive characteristics of DER, resulting in surges, failures, and other grid malfunctions [1, 2, 3]. Once an abnormal event occurs, emergency control operations necessitate early detection and quick location of the event to timely recover to the normal conditions. Undetected failures/sparks from the power grid near vulnerable vegetation have regularly ranked among the top identified initiators of devastating wildfires in the past [4].

However, localizing faults in distribution systems in real-time is faced with several practical challenges: low observability, unbalanced load, three-phase measurements, and the stochastic ambient environments due to load variations and topology changes [5, 6, 7]. In the light of these challenges, we

can distinguish fault localization methods in the literature into two categories. The traditional approaches employ protection devices [8, 9, 10], such as relays, circuit breakers, and fault indicators, to locate nearby faults. Unfortunately, many reports indicate the defects and lose-coordination concerning these devices in existing power grids with a high penetration of DERs [1, 2, 6]. Another category is based on network-wide measurements [11, 12, 13]. For example, the impedance-based approach can exactly estimate the fault distance for local networks, but they are sensitive to the inaccuracy of load models, line parameters. Traveling-wave-based approaches have also been applied for fault localization, but the high cost of installing and maintaining the measuring instruments everywhere hinders their extensive application to large-scale networks [13].

In recent years, distribution grid real-time observability has improved due to the installation of various wide-area sensors, such as advanced metering infrastructures (AMIs), phasor measurement units (PMU) [14], and micro-phasor measurement unit (μ PMUs) [15] that motivates the data-driven fault detection [16] and localization [17, 18, 19, 20, 21, 22, 23, 24]. For example, researchers have formulated a sparse optimization problem to locate faults based on the compressed sensing theory [18, 19, 20]. However, the accurate solution often requires the measurements to have high sampling rates (e.g., 4k Hz [20]) and reliable admittance matrix values of the grid that may not be guaranteed. Furthermore, the convergence of the estimation algorithm still requires a high ratio of measured buses. Similarly, supervised machine learning-based algorithms have been proposed to efficiently locate faults [17, 21, 22, 23, 25, 26]. However, these measurement-based approaches either require the full observation of networks or a sufficient number of labeled datasets for training. However, realistic historical data collected from distribution grid meters are often *not well documented or labeled*, which diminishes the performance of such supervised methods. Crucially, several proposed machine learning algorithms lack clear physical interpretation and hence their performance is vulnerable to stochastic ambient environments that arise in distribution grids due to random load variations and topology changes. This situation begs the question: *Can we employ the unique physics of power grids to inform supervised data-driven fault localization algorithms and augment their robustness to challenges associated with practical grid data?*

In this paper, we are thus interested in fault localization in distribution grids, in the challenging but realistic regime of (a) sparse observation, and (b) system variability, with (c) low ratios of labeled training data. To overcome these issues, we

The authors acknowledge the support from the Department of Energy through the Advanced Grid Modeling (AGM) Program, and the Center for Non Linear Studies (CNLS) at Los Alamos National Laboratory.

W. Li and D. Deka are with the Theoretical Division and Center for Non-Linear Studies (CNLS), Los Alamos National Laboratory, Los Alamos, NM, USA. Email: {wenting, deepjyoti}@lanl.gov

propose a *physics and statistics informed* graph neural-network (GNN) architecture that has demonstrably better performance for fault localization in realistic observability regimes. One key of our approach is to take advantage of the *unique capability* of GNN to learn data under the constraint of the power grid topology and physical correlations.

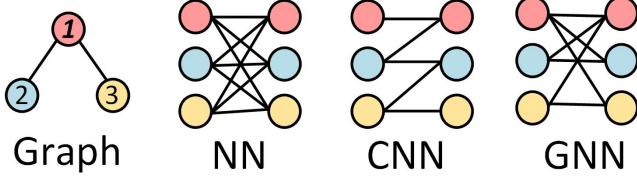


Fig. 1: The connectivity between layers in the NN and CNN fails to reflect the topological relations of the three nodes, but GNN captures the local structure of the original graph.

GNNs are a class of neural networks that efficiently map graphical data into node embedding in low-dimensional space to represent both the node features and graph structure simultaneously [27]. GNN has brought breakthroughs to the structured data in the domains of recommendation networks, biological structures, and social networks [28, 29]. The focal point of GNN to stand out of the conventional neural networks is its capability to encode the neighborhood structure in the underlying graph through the connectivity between hidden layers, as shown in Fig. 1. Thus, GNN can be designed to control the flow of information between neighboring nodal variables in the power grid, or between datasets that have strong statistical correlations (using a similarity graph on available data). We use this feature particularly to encode the grid topology and the physical relations between nodes in our learning algorithm.

Our contributions: This paper formulates a two-stage graph neural network architecture to locate faults in distribution systems with low observability and stochastic environments, using a small number of labeled data for training. Precisely, to address the issue of low observability, We inform \mathcal{G}_I (GNN in the first stage) with the structure of the distribution grid by constructing an adjustable and novel adjacency matrix A . Meanwhile, in the second stage \mathcal{G}_{II} , we use a different adjacency matrix B based on the statistical similarity of labeled and unlabeled datasets. This second GNN improves the localization accuracy when label rates are low. We theoretically interpret the functions of adjacency matrices A and B in stages I and II respectively, through equivalence with random walks. The proposed framework is validated in the IEEE 37 and 123-node test feeders [30, 31] in various scenarios through OpenDSS software [32]. Our approach outperforms the existing algorithms by significant margins in accuracy and robustness to low label rates, load variations, and topology changes.

The remaining parts are organized as follows: Section II introduces the vital physics behind data that motivates us to build our physics-informed graph model for fault location, and then we formulate the problem for the sake of some practical challenges. Sequentially, we present the two-stage

graph learning framework in Section III. The following section explains the principles of graph learning, demonstrating the benefits of the constructed adjacency matrices A, B in the two stages. Section V validates the effectiveness and advantages of our approach, comparing with state of the art. Finally, the conclusions and future works are discussed in Section VI.

II. SPARSITY OF FAULT CURRENTS AND PROBLEM FORMULATION

Consider a power grid with n nodes in the set \mathcal{V} and l branches in \mathcal{E} , where the voltages and currents of s nodes in the set Ω are measured by micro-phase measurement units (μ PMUs). Once a fault occurs, the faulty position is treated as the label of this event. Interestingly, the nodal fault currents show approximately sparse variations that the nonzero values are closely related to the fault positions or labels [18, 19, 20]. In this section, we will derive the sparsity property physically to explain how the physical laws reduce the label requirement, which in turn enables fault localization in a challenging but practical regime.

A. Sparsity of Fault Currents

We analyze voltages and currents in three-phase complex numbers domain. When a fault occurs at a point f (equivalent to a node) between the nodes i and $j, j > i$, the voltages and currents at the faulty point and the node $i \neq f, i \in [1, n]$ are $u_f^{abc}, c_f^{abc}, u_i^{abc}, c_i^{abc} \in \mathbb{C}^{3 \times 1}$ respectively. $Y_{ij} \in \mathbb{C}^{3 \times 3}$ is the admittance matrix between nodes i and j before the fault while Y'_{ij} is that after the fault. According to the Kirchhoff's law and the substitution theory [7, 33], we have

$$\begin{bmatrix} Y_{11} & \cdots & \cdots & \cdots & Y_{1n} & \mathbf{0} \\ \cdots & \cdots & \cdots & \cdots & \cdots & \mathbf{0} \\ \cdots & Y'_{ii} & \cdots & Y'_{ij} & \cdots & Y'_{if} \\ \cdots & \cdots & \cdots & \cdots & \cdots & \mathbf{0} \\ \cdots & Y'_{ji} & \cdots & Y'_{jj} & \cdots & Y'_{jf} \\ \cdots & \cdots & \cdots & \cdots & \cdots & \mathbf{0} \\ Y_{n1} & \cdots & \cdots & \cdots & Y_{nn} & \mathbf{0} \\ \mathbf{0} & Y'_{fi} & \mathbf{0} & Y'_{fj} & \mathbf{0} & Y'_{ff} \end{bmatrix} \begin{bmatrix} u_1^{abc} \\ \cdots \\ u_i^{abc} \\ \cdots \\ u_j^{abc} \\ \cdots \\ u_n^{abc} \\ u_f^{abc} \end{bmatrix} = \begin{bmatrix} c_1^{abc} \\ \cdots \\ c_i^{abc} \\ \cdots \\ c_j^{abc} \\ \cdots \\ c_n^{abc} \\ c_f^{abc} \end{bmatrix} \quad (1)$$

We obtain the equivalence of (1) by replacing Y'_{ij} with $Y_{ij} - (Y_{ij} - Y'_{ij})$ as

$$\begin{bmatrix} Y_{11} & \cdots & \cdots & \cdots & Y_{1n} \\ \cdots & \cdots & \cdots & \cdots & \cdots \\ \cdots & Y_{ii} & \cdots & Y_{ij} & \cdots \\ \cdots & \cdots & \cdots & \cdots & \cdots \\ \cdots & Y_{ji} & \cdots & Y_{jj} & \cdots \\ \cdots & \cdots & \cdots & \cdots & \cdots \\ Y_{n1} & \cdots & \cdots & \cdots & Y_{nn} \end{bmatrix} \begin{bmatrix} u_1^{abc} \\ \cdots \\ u_i^{abc} \\ \cdots \\ u_j^{abc} \\ \cdots \\ u_n^{abc} \end{bmatrix} - \begin{bmatrix} 0 \\ \cdots \\ \delta_i^{abc} \\ \cdots \\ \delta_j^{abc} \\ \cdots \\ 0 \end{bmatrix} = \begin{bmatrix} c_1^{abc} \\ \cdots \\ c_i^{abc} \\ \cdots \\ c_j^{abc} \\ \cdots \\ c_n^{abc} \end{bmatrix} \Rightarrow YU - \Delta_{ij} = C \quad (2)$$

where $\delta_i^{abc} = (Y_{ii} - Y'_{ii})u_i^{abc} + (Y_{ij} - Y'_{ij})u_j^{abc}$, $\delta_j^{abc} = (Y_{ji} - Y'_{ji})u_i^{abc} + (Y_{jj} - Y'_{jj})u_j^{abc}$. Notice that $\Delta_{ij} \in \mathbb{C}^{3n}$ is a *sparse vector with the nonzero values corresponding to the two terminals i, j of the faulted line*.

We also know that U_0, C_0 , the voltages and currents on normal conditions, satisfy that $YU_0 = C_0$. Let $\Delta U = U -$

ΔU , $\Delta C = C - C_0$, and we acquire the interpretation of voltage variations weighted by Y from (2), i.e.,

$$Y \Delta U = \Delta C + \Delta_{ij} \quad (3)$$

Remarks: As Y is a sparse matrix, whose nonzero values correspond to the connected nodes, the product of Y and ΔU , on the left side of (3), equals the linear combination of the node k 's neighbors weighted by the admittance, i.e., $\sum_{j \in \mathcal{N}_k} Y_{kj} \Delta u_j^{abc}$, $k = 1, \dots, n$, where \mathcal{N}_k denotes the set of nodes connected with k . On the right side of (3), we discover that the physical interpretation of these linear combinations is the summation of ΔC and Δ_{ij} . Among them, Δ_{ij} is dominant and ΔC is trivial since load variations at this moment are supposed not to be drastic [6, 7]. Notice that Δ_{ij} only has nonzero values at the nodes i, j connected with the fault point, causing the dominant entries of $\Delta C + \Delta_{ij}$ to closely relate to the fault location, provided sufficient measurements are available. While it may not be sufficient in the low observability regime we are interested in, ΔU can help guide our search for the correct fault estimate.

B. Problem Formulation

We consider a N length data-set of three phase voltage measurements from $s < n$ measured nodes in the grid, i.e., $X^p \in R^{n \times 6} = [V^a, \theta^a, V^b, \theta^b, V^c, \theta^c]$, $p = 1, \dots, N$. Here unmeasured nodes are given a value 0. Additionally, we have partial labels denoting the location of the faults, $y^p \in \{1, \dots, c\}$ for some datasets $p = 1, \dots, m$, where $m \ll N$. We target at efficiently predicting the location of unknown faults regardless of fault types and fault impedance. Note that $m \ll N$ implies that only a few number of datasets are labeled with the true fault location while others are not.

Fault location can be equivalent to be a classification problem [21], but practically this classifier faces more challenges: power grids are not fully measured, not many datasets are labeled, and the ambient environment is stochastic due to load fluctuations and topology changes. Though Section II-A demonstrates the effect of power system topology in estimating faults via ΔU , the sparse observation of power network hinders the way of directly applying GNN on the the power grid topology. Furthermore, the non-static measurements of power grids demand the classifier to be robust to the out of distribution data (ODD) [34], due to changing load dispatch, random fault impedance, and topology changes.

The next section will present our treatment of these issues by constructing a two-stage graph learning framework.

III. PROPOSED GRAPH LEARNING FRAMEWORK

Fig. 2 shows our two-stage graph learning framework for fault location. In Stage I, we construct a graph neural network \mathcal{G}_I to efficiently predict fault location in *real-time* by learning a graph embedding of power grid topology, which represents both the node features and topology structure. Two distinctions of our \mathcal{G}_I are the *adjustable adjacency matrix* and the *global transformation* layer. The former, separate from the conventional GNN [28, 29], handles the challenges of sparse observability while the latter is equivalent to a decoder

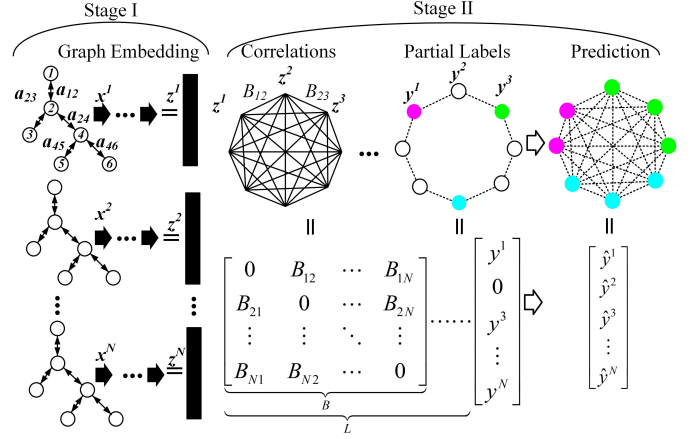


Fig. 2: The structure of our graph learning framework of two stages

that maps the hidden variables of the whole graph to the location prediction. Following Stage I, we design the Stage II with another graph neural network \mathcal{G}_{II} using correlations between the available labeled and unlabeled datasets, to further improve the location accuracy. The novel adjacency matrix in \mathcal{G}_{II} is based on the learnt graph embedding from Stage I. The detailed theoretical analysis of these two adjacency matrices for \mathcal{G}_I and \mathcal{G}_{II} is presented in Section IV.

A. Stage I: Graph Embedding Learning

When the measured nodes of the power grid are sparse, it is difficult to learn informative embedding of the node without measured neighbors. Instead, our key idea is to construct an adjacency matrix $A \in R^{n \times n}$ based on the shortest distance between any pair of nodes to ensure that each node is observable. Then we accomplish graph embedding with two major procedures: local aggregation and global transformation.

Construct Adjacency Matrix A : We construct A through the Gaussian kernel learning using the k_1 nearest neighbors [35].

$$a_{ij} = \begin{cases} \exp(-\frac{d_{ij}^2}{\delta_i^2}) & \text{if } j \in \mathcal{N}_i^{k_1} \\ 0 & \text{else} \end{cases} \quad (4)$$

where d_{ij} is the shortest distance between nodes i, j , $\delta_i = \frac{1}{k_1} \sum_{j \in \mathcal{N}_i^{k_1}} d_{ij}$, and $\mathcal{N}_i^{k_1}$ consists of the k_1 nearest neighbors of node i . We symmetrize the matrix A by $a_{ij} = \max(a_{ij}, a_{ji})$ treating power grid topology as an undirected graph. Note that k_1 can be adjusted to ensure at least each node has one observed neighbor, particularly when the observation is very sparse. A large k_1 causes each node to be influenced by a wider region while a small k_1 narrows down the size of the neighborhood.

1) *Local Aggregation:* K hidden layers map the p th data matrix X^p into hidden variables $H^k \in R^{n \times n_k} = [h_1^k, \dots, h_n^k]$, $k = 1, \dots, K$ with the shared weight matrix $W^k \in R^{2n_{k-1} \times n_k}$ among all nodes, and $H^0 = X^p$. The update rule of the k th layer is:

$$h_i^k = \sigma(\{h_i^{k-1} \parallel \text{Aggregate}_{j \in \mathcal{N}_i}(h_j^{k-1} \tilde{a}_{ij})\} W^k) \quad (5)$$

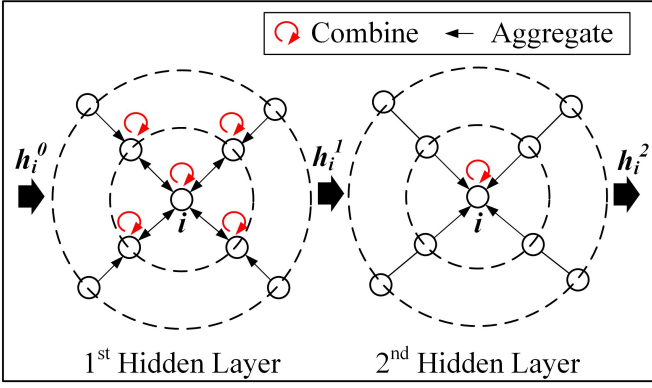


Fig. 3: Example when $K = 2$: In the first layer, node i aggregates information from its 1-hop neighbors and itself to obtain h_i^1 (other nodes update similarly); in the 2nd hidden layer, node i equivalently receives information from 2-hop neighbors to produce h_i^2 .

where \parallel means to concatenate the two vectors, $\text{Aggregate}_{j \in \mathcal{N}_i}(h_j^{k-1} \tilde{a}_{ij}) = \frac{1}{|\mathcal{N}_i|} \sum_{j \in \mathcal{N}_i} (h_j^{k-1} \tilde{a}_{ij})$, $\sigma(x) = \max(0, x)$, \tilde{a}_{ij} is the normalized a_{ij} such that $\sum_{j \in \mathcal{N}_i} \tilde{a}_{ij} = 1$, and the \mathcal{N}_i is the neighborhood of node i . A two-layer illustration is in Fig. 3. Note that instead of utilizing all the nodes in \mathcal{N}_i , an alternation is to sample partial neighbors [27].

2) *Global Transformation*: Global transformation converts the hidden variables of all the local nodes into prediction probability of the whole data sample as the graph embedding. Firstly, the vectorized hidden variables $\hat{h}^K \in R^{n_K}$ go through fully connected layers with the trainable weights $W^f \in R^{n_K \times 2n}$, $b^f \in R^{2n}$, $W^o \in R^{2n \times n}$, $b^o \in R^n$ to become the vector $f \in R^n$. Then the output layer transforms f into graph embedding $z^p \in [0, 1]^n$ with $W^o \in R^{2n \times n}$, $b^o \in R^n$ for the p th data sample as follows,

$$z_i^p = \frac{\exp(f_i)}{\sum_{j=1}^n \exp(f_j)}, \quad f = (\hat{h}^K W^f + b^f) W^o + b^o \quad (6)$$

where z_i^p, f_i are the i th entry of z^p and f respectively.

3) *Loss Function of Stage I*:

$$(\Theta_1) = -\sum_{p=1}^m y^p \log(z^p) + \lambda_1 \|\Theta_1\| \quad (7)$$

The first term of (7) is the cross entropy of y^p and z^p for available labeled data samples, and the second is the regularization term to augment the generalization capability, where $\|\Theta_1\|$ is the l_2 -norm of all the trainable parameters $\Theta^I = \{W^1, \dots, W^K, W^f, b^f, W^o, b^o\}$ of \mathcal{G}_1 with the hyper-parameter λ_1 . By minimizing (7), the Θ_1 is automatically learned by back-propagation.

4) *Practical Implementation Technique in Training*: The learned graph embedding z^p is influenced by the two components of \mathcal{G}_1 : the *local aggregation* and the *global transformation*. To accelerate the convergence, we are inspired by [36] to alternatively train these components with two hyper-parameters T_1, T_2 . Specifically, we first optimize both components for T_1 epochs. Second, we fix the weights $W^k, k = 1, \dots, K$ to train only the *global transformation* component by minimizing the loss in (7) for T_2 epochs. Then repeat

these two steps until the early stop or the maximum iterations are reached [37]. Empirically, this alternative training speeds up the convergence and accomplishes higher classification accuracy. The detailed discussion is in Section V-G.

B. Stage II: Label Propagation

To further increase the location accuracy when given a number of unlabeled datasets, we build the correlation matrix $B \in R^{N \times N}$ of the labeled and unlabeled datasets as the adjacency matrix of the graph \mathcal{G}_{II} . Note that each vertex of \mathcal{G}_{II} represents one data sample. The intuition is that the faults occur at the same or nearby location share similar physical characteristics referring to the analysis in Section II-A, resulting in similarity of datasets. Our graph model \mathcal{G}_{II} employs B to propagate the labels to the unlabeled data samples through graph convolutional layers (GCL) [28] followed by the output layer.

Construct Adjacency Matrix B : The critical purpose of our B is to learn useful correlations among data samples while cutting off misleading correlations. For that we use z^p , the output of Stage I. Precisely, we first zero out the entries of z^p that correspond to nodes far beyond the Stage I predicted location $p^* = \arg \max_i z_i^p$, and obtain vector \hat{z}^p . Let \mathcal{S}_{p^*} be the set of nodes physically connected with p^* in the original power grid. Then

$$\hat{z}_k^p = \begin{cases} 0 & \text{if } k \notin \mathcal{S}_{p^*} \\ z_k^p & \text{otherwise} \end{cases} \quad (8)$$

Second, we calculate the similarity $s(p, q)$ of embedding between any pair of data samples \hat{z}^p, \hat{z}^q through distance metrics. Here we apply the subspace angle $s(p, q) = \frac{(\hat{z}^p, \hat{z}^q)}{\|\hat{z}^p\|_2 \|\hat{z}^q\|_2}$ [38] as distance metric. The entry at the p th row and q th column of B is then defined as

$$B_{pq} = \begin{cases} s(p, q) & \text{if } q, p \text{ are similar to each other} \\ 0 & \text{else} \end{cases} \quad (9)$$

where “ q, p are similar to each other” means that the $s(p, q)$ is among the largest k_{II} values of $\{s(p, q'), q' \in [1, N]\}$ or $\{s(p', q), p' \in [1, N]\}$. Significantly, B becomes a sparse matrix with non-zero entries restricted to data-points at close graphical locations. This helps accelerate the training process when $k_{II} \ll N$. We give a theoretical explanation for B in Section IV-B. Once B is estimated, we use it in a Graph Convolutional Network.

1) *Graph Convolutional Layers*: Reshape all the raw data samples $X^p, p = 1, \dots, N$ to form matrix $C^0 \in R^{N \times 6n}$ as the input of the Graph Convolutional Layers (GCL).

$$C^l = \sigma(D^{-\frac{1}{2}} \hat{B} D^{-\frac{1}{2}} C^{l-1} W_{II}^l) \quad (10)$$

where $C^l, l = 1, \dots, L$ is the l th output of the hidden layer with weights $W_{II}^l \in R^{n_{l-1} \times n_l}$, $\hat{B} = I_N + B$ and D is the degree matrix corresponding to \hat{B} for normalization.

2) *Output layer*: The output layer performs the linear regression on the c^p , the p th row of C^L , with the weight $W_{\Pi}^o \in R^{n_L \times n}$ and the bias $b_{\Pi}^o \in R^n$ to obtain $g^p \in R^n$, and then converts g^p to be the prediction probability $\hat{y}^p \in R^n$ through a softmax function as follows,

$$\hat{y}_i^p = \frac{\exp(g_i^p)}{\sum_{j=1}^n \exp(g_j^p)}, \quad g^p = c^p W_{\Pi}^o + b_{\Pi}^o \quad (11)$$

where \hat{y}_i^p, g_i^p are the i th entry of \hat{y}^p and g^p respectively.

3) *Loss function of Stage II*: We use the regularized cross entropy loss function as

$$\ell(\Theta_{\Pi}) = -\sum_{p=1}^m y^p \log(\hat{y}^p) + \lambda_{\Pi} \|\Theta_{\Pi}\| \quad (12)$$

where $\Theta_{\Pi} = \{W_{\Pi}^1, \dots, W_{\Pi}^L, W_{\Pi}^o, b^o\}$ includes all the trainable parameters of \mathcal{G}_{Π} .

C. Training Complexity of the Framework

For Stage I, the time complexity of the local aggregation in (5) is $O(Knk_1r + Knr^2)$, where $r = \max_{k=0}^K (n_k)$, and that of the global transformation in (6) is $O(n^2r)$. Moreover, the hyper-parameter $k_1 \ll n$ if the measured nodes are evenly distributed to ensure each node has an observed node nearby in the network. In stage II, the dimension of B becomes high when N is large, but the time complexity can be reduced by choosing a relatively small k_{Π} since B is a sparse matrix defined by k_{Π} . By employing the efficiency of sparse multiplication, the computational complexity is $O(LNk_{\Pi}\hat{r} + LN\hat{r}^2)$, where $\hat{r} = \max_{l=0}^L (n_l)$.

IV. THEORETICAL INTERPRETATIONS

Directly understanding how the graph neural networks learn the node embedding is laborious, but the influences of input on the hidden variables of the k th graph neural network layer can be equivalent to the expectation of random walk distribution [39, 40, 41]. Here a walk starts from one node and randomly steps into the other k nodes according to the adjacency matrix. Consequently, the advantages of A and B in augmenting visibility and location accuracy become clear through understanding the paths of random walks.

A. Construct A to Improve Visibility

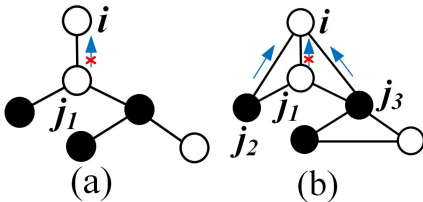


Fig. 4: Example: The filled nodes are measured while the void nodes are unmeasured. When $k_1 = 2, K = 1$, node i only has one connected node j_1 in (a), but i has three neighbors $j_k, k = 1, 2, 3$ in (b) defined by our A . Though the node i and its immediate neighbor j_1 both are unmeasured, we still have two paths to reach node i in (b)

Node Influence of \mathcal{G}_I : The node influence, denoted as $I(h_i^k, h_j^0; k)$, measures the influences of the node j 's input, h_j^0 ,

on node i 's learned hidden variable, h_i^k after k layers [39, 40], which quantifies the variations of h_i^k when h_j^0 changes,

$$\begin{aligned} I(h_i^k, h_j^0; k) &= \partial h_i^k / \partial h_j^0 \\ &= \text{Pr}(\text{Walk from } i \text{ to } j \text{ with } k \text{ steps}) \\ &= \sum_{\mathcal{P} \in \mathcal{P}_k^{i \rightarrow j}} \prod_{e \in \mathcal{P}} \tilde{a}_e \end{aligned} \quad (13)$$

where Pr is the abbreviation of probability, $\mathcal{P}_k^{i \rightarrow j}$ represents the path from i to j with k steps, a_e is the weight of the edge e defined by A that $\tilde{a}_e = \tilde{a}_{i'j'}$ when $e = (i', j')$. As the learning process of each layer is independent, the probability of choosing one path \mathcal{P} is the product of $\tilde{a}_e, e \in \mathcal{P}$.

The information collected by each node via \mathcal{G}_I is implied by the total influence $I(h_i^K)$,

$$\begin{aligned} I(h_i^K) &= \sum_{j \in \mathcal{N}_i^K, j \in \Omega} I(h_i^K, h_j^0; K) \\ &= \sum_{j \in \mathcal{N}_i^K, j \in \Omega} \sum_{\mathcal{P} \in \mathcal{P}_K^{i \rightarrow j}} \prod_{e \in \mathcal{P}} \tilde{a}_e \end{aligned} \quad (14)$$

where \mathcal{N}_i^K denotes the K -hop neighborhood of node i , Ω is the set of measured nodes. The information obtained at node i is rich if more paths from the observed nodes to node i .

Low observability of power grids brings challenges to the embedding learning of the unmeasured nodes in stage I: if we intuitively construct the adjacency matrix according to power grid topology or admittance matrix, then \mathcal{G}_I may fail to observe some unmeasured nodes when no path within K steps reaching them, leading to some trivial node embedding. Fig. 4 (a) shows one simple example that the nodes with K -hop away from node i are unmeasured.

If GNNs are sufficiently deep, each node can receive information from a much widespread region through long random walks, but *deep* GNNs have technical bottlenecks to show satisfactory performance [27]. Our treatment is to construct A in (4) employing shortest distances and obtain a reduced graph that each node is observable from some path. In this way, h_i^k of the unmeasured node i successfully captures the information passing from those measured neighbors, as illustrated in Fig. 4 (b). In the original graph in Fig. 4 (a), no path from measured nodes arrives at node i with K steps, but in (b) j_2, j_3 are also node i 's K -hop neighbors that can deliver local structure information to formulate useful node embedding of node i .

B. Construct B to Enhance the Exact Prediction Probability

B characterizes the correlations of labeled and unlabeled data samples to improve the prediction probability. We first show the random-walk interpretation of the node score in \mathcal{G}_{Π} , and then introduce how we increase correct prediction probability by cutting off misleading correlations. The effects of B are also validated by experiments in Section V-D.

Node Influence of \mathcal{G}_{Π} : In \mathcal{G}_{Π} , the p th node corresponds to the data sample X^p , and we care about the influence of the known labeled data samples on the unlabeled ones. The node

influence of the labeled data sample q on the unlabeled data sample p after l layers is $I'(C_p^l, C_q^0; l)$.

$$\begin{aligned} I'(C_p^l, C_q^0; l) &= \partial C_p^l / \partial C_q^0 \\ &= \Pr(\text{Walk from } p \text{ to } q \text{ with } l \text{ steps}) \\ &= \sum_{\mathcal{P} \in \mathcal{P}_l^{p \rightarrow q}} \prod_{e \in \mathcal{P}} \bar{B}_e \end{aligned} \quad (15)$$

where $\bar{B}_e = \bar{B}_{p'q'}$, $e = (p', q')$ is the edge e between p' and q' , and $\bar{B}_{p'q'}$ is the normalized weight that $\sum_{q'=1}^N \bar{B}_{p'q'} = 1$.

According to the Theory 1 in [39], the expectation of the total influence of node q on p after L hidden layers, $I'_p(q; L) = \sum_q I'(C_p^L, C_q^0; L) / \sum_r I'(C_p^L, C_r^0; L)$, is equivalent to the probability that data sample p has the same label with q after L -step random walk, i.e.,

$$\Pr(\hat{y}^p = y^p) = E\left(\frac{\sum_{q: y^q = y^p} I'(C_p^L, C_q^0; L)}{\sum_{r: y^r \in [1, c]} I'(C_p^L, C_r^0; L)}\right) \quad (16)$$

$$= E\left(\frac{\sum_{q: y^q = y^p} \sum_{\mathcal{P} \in \mathcal{P}_L^{p \rightarrow q}} \prod_{e \in \mathcal{P}} \bar{B}_e}{\sum_{r: y^r \in [1, c]} \sum_{\mathcal{P} \in \mathcal{P}_L^{p \rightarrow r}} \prod_{e \in \mathcal{P}} \bar{B}_e}\right) \quad (17)$$

where $q : y^q = y^p$ denotes those data samples q have the same labels with y^p , and $r : y^r \in [1, c]$ represents any data sample r . Hence, the correct prediction of the unlabeled data sample p has high probability if (1) The paths from the data samples with the same labels y^p are more than those with other labels; (2) the number of labeled data samples with y^p is significant.

Cut off the Unrelated Paths through B : We construct B via $\hat{z}^p, p = 1, \dots, N$ rather than the raw datasets X^p to produce more zero entries that cut off the paths from mismatching labels, resulting in an increase in the accurate prediction probability. If we calculate B with X^p , the correct prediction probability $\Pr(\hat{y}^p = y^p)$ is given by (16). However, if we use \hat{z}^p as input, it is clear from (8) and (9) that $s(p, q)$ for datasets p, q is nonzero only if the prediction q^* and p^* are within two-hops of each other. Thus, the physical distance between the true labels of data-set p and q should be within four hops if $s(p, q)$ is not zero. The correct prediction probability, in that case, is thus larger as the p th data sample only has the access to partial data samples r whose true labels $y^r \in \mathcal{N}_{y^p}^{4L}$, i.e.,

$$P'(\hat{y}^p = y^p) = E\left(\frac{\sum_{q: y^q = y^p} I'(X^p, X^q; L)}{\sum_{r: y^r \in \mathcal{N}_{y^p}^{4L}} I'(X^p, X^r; L)}\right) \geq \Pr(\hat{y}^p = y^p)$$

As we also control the total number of nonzero values of each row of B to be no more than $2k_{II}$, thus $|\mathcal{N}_{y^p}^{4L}| \leq 2k_{II} < |\mathcal{V}|$, where $|\cdot|$ denotes the size of a set. Therefore, we improve the correct prediction probability by constructing B using the learned graph embedding.

V. NUMERICAL EXPERIMENTS

We first implement the proposed framework in the 123-node test feeder [31], simulated by OpenDSS. This test feeder is typically composed of voltage regulators, overhead/underground lines, three-phase switch shunts, and unbalancing loads. Our approach shows high performance for various types of faults

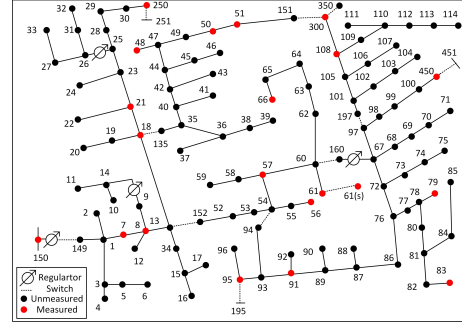


Fig. 5: The IEEE 123-bus test feeder [31]

at low label rates, outperforming three well-known baselines, described later, by significant margins. Moreover, we validate the robustness to topology changes and load variations, and analyze the effects of different stages, alternative adjacency matrices and misclassification. In addition, our graph learning framework can easily adapt to another distribution system, the IEEE 37-node test feeder [30], where we demonstrate the superior location performance using the proposed training strategy in Section III-A4.

A. Implementation Details and Performance Metrics

The graphical structure our testing system is shown in Fig. 5, where 21 out of the 128 nodes are measured marked as red. Nine pairs of nodes are connected by switches or regulators at the same locations. Thus a total of 119 possible faulty positions exist, which are represented by the labels $y^p \in \{1, \dots, c\}, c = 119$. We simulate $N = 24480$ data samples including single phase to ground (SPG) faults, phase to phase (PP) faults, and Double-phase to ground (DPG) faults at all the three phase nodes with fault impedance varying from $0.05\Omega \sim 20\Omega$. All the loads are made to fluctuate following the typical probabilistic distribution from OpenDSS loadshape database. The expectation of the load variation at one node is 0.53 per unit (p.u.). Each data sample is a matrix $X^p \in R^{128 \times 6}$, where only measured nodes have nonzero values. To validate the robustness to ODD, we simulate another 110160 datasets when the system topology or load varies. We normalize each dataset X^p by subtracting the mean values and scaling with the standard deviation of all datasets.

1) Structures of $\mathcal{G}_I, \mathcal{G}_{II}$: \mathcal{G}_I has three hidden layers with $W^k \in R^{32 \times 32}, n_k = 32, k = 1, \dots, K = 3$. We set $k_I = 3 \ll n$ considering the sparse infrastructure of distribution systems, to construct matrix A (see Eq. 4). The hyper-parameters $\lambda_I = 5 \times 10^{-3}, T_1 = 10, T_2 = 10$, and the learning rate is 0.001. \mathcal{G}_{II} has two layers with $n_l = 3n$ for $l = 1, 2$. We take hyper-parameter $k_{II} = 120$ for B (see Eq. 9). The learning rate for \mathcal{G}_{II} is 0.001 and $\lambda_{II} = 5 \times 10^{-5}$. We implement the proposed structure through Pytorch [42]. Based on a MacBook Pro with CPU of 2.4 GHz 8-core Intel i9 series, memory of 32 GB, the per-iteration running time of the proposed graph neural network \mathcal{G}_I is 0.03 seconds, which becomes 0.02 seconds if using 1 NVIDIA Tesla GPU.

2) *Performance Metrics* : We adapt three performance metrics: F1-score, location accuracy rate (LAR), and LAR^{1-hop} [43]. The definitions of these three metrics are based on four basic concepts: True Positive (TP_i) is the number of correctly predicted samples of location i ; False Positive (FP_i) is the number of wrongly predicted samples of location i ; True Negative (TN_i) is the number of correctly predicted samples of locations rather than i ; False Negative (FN_i) is the number of wrongly predicted samples of locations rather than i . Then

$$\begin{aligned}
 P_i &= \frac{TP_i}{TP_i + FP_i} \quad (\text{Precision}), \\
 R_i &= \frac{TP_i}{TP_i + FN_i} \quad (\text{Recall}), \\
 F_i &= 2R_iP_i/(R_i + P_i) \quad (\text{F1-score}), \\
 LAR_i &= TP_i/(TP_i + FP_i + TN_i + FN_i), \text{ and} \\
 LAR_i^{1-hop} &= TP'_i/(TP_i + FP_i + TN_i + FN_i) \quad (18)
 \end{aligned}$$

where TP'_i denotes that the number of data samples where the predicted node is in the immediate neighborhood of the true faulty node i . The notations LAR and LAR^{1-hop} are the average of LAR_i and LAR_i^{1-hop} , $i \in [1, c]$ of all the locations.

B. Location Performance

Table I: Location Performance of All Types

Label Rate β	75%	50%	25%	15%
F1 Score (%)	98.7	98.5	98.4	97.6
LAR (%)	99.0	98.8	98.7	98.0
LAR^{1-hop} (%)	100.0	100.0	99.96	99.90
Unmeasured Nodes	1	1	1, 89	1, 89
Measured Nodes	51,7,91	51,7	51,7	51

We train \mathcal{G}_1 at different label rates β , which is the ratio of the number of training data samples to N . Table I reports the location performance in terms of the three metrics when β varies from 75% to 15%. F1 Scores and LARs of our model are stable and remain higher than 97% even only $\beta = 15\%$. Note that the labeled data samples for training are randomly selected for each location to avoid the issue of data imbalance [44]. Crucially, the LAR^{1-hop} is close to 100%, indicating that the predicted node is in the 1-hop neighborhood of the faulty node with a high probability.

Misclassification Analysis: We summarize the fault locations that have more than 5% prediction errors in the last two lines of Table I, where “Unmeasured Nodes” indicates those locations are not directly measured, while “Measured Nodes” means they are measured. The main reason for the misclassification of “Unmeasured Nodes” is the lack of information since we can only learn these nodes from their neighbors, but when we increase the β from 15% to 75%, the prediction errors reduce for those “Unmeasured Nodes”. Rather, increasing label rates shows no obvious benefits on those “Measured Nodes” because faults at these locations share some similar features with other fault locations. More training datasets potentially cause faults at distinctive nodes to have close features. This issue can be mitigated in multiple ways. For example, we can optimize the placement of sensors by maximizing the distinction of faults at various location;

or enrich the complexity of inputs by incorporating multi-source information. These will be a potential future research direction to further enhance the reliability of our approach in more extensive situations.

C. Performance Comparison at Various Label Rates

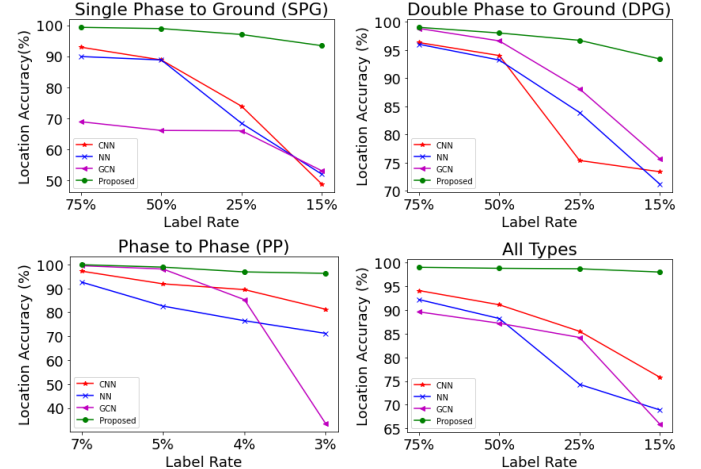


Fig. 6: Comparison of the Location Accuracy at Different Label Rates

We compare our model with three baseline classifiers (CNN, NN, GCN) in Fig. 6, which includes the location performance for different types of faults respectively. Note that the power grid operator can first determine the type of each fault by other approaches, such as [45, 46]. When training the model with a very low label rate (less than 4%), we set $k_1 = 2$ to reach slightly better performance.

We find that when the label rates are high, some classifiers achieve comparable performance with the proposed model, but their LARs decline dramatically when label rates become low. On the contrary, the proposed algorithm, primarily due to Stage II, shows more stable and accurate performance, outperforming the baselines by significant margins at realistic low label rates. Next we will separate the location performance at the two stages to demonstrate their effectiveness respectively.

D. Performance at Different Stages When Label Rates are Low

Table II: Location Performance of Different Stages

Types of Faults	SPG	PPG	PP
Label Rate	15%	15%	3%
Stage I Only (LAR)	92.9	92.7	95.7
Stage II Only (LAR)	30.7	39.6	78.2
Stage I + II (LAR)	93.3	93.5	96.3
Stage I Only (LAR^{1-hop})	94.8	95.1	96.6
Stage II Only (LAR^{1-hop})	37.3	46.3	82.3
Stage I + II (LAR^{1-hop})	99.7	98.9	99.8

Table II shows the performances at different stages when label rates are low, where “Stage I Only” denotes that we only train \mathcal{G}_1 to locate faults; “Stage II Only” means that we directly utilize the input data X^p rather than the embedding z^p to construct the matrix B and then locate the unknown faults. Note that “Stage II Only” is the typical manner of label

propagation strategy for the semi-supervised learning in the computer vision domain [47]. “Stage I + II” represents our proposed graph learning framework.

Comparing with the “Stage I Only” and “Stage II Only”, we observe the superior performance of combining stage I and II. Also, the low LAR of “Stage II Only” indicates the significance of constructing B using z^p rather than X^p . The high accuracy of “Stage I Only” ensures the learned z^p is reliable. Therefore, combination of the stages I and II benefits the location accuracy further.

E. Robustness to Out of Distribution Data

We validate the robustness of different classifiers to ODD data due to load variations and topology changes. Note that the performance of each classifier here is for the best model in Fig. 6, *but without retraining*.

Table III demonstrates the robustness to load variations, where Δp denotes the averaged load variation per unit (p.u.) at each node with a load. The Δp for training data is 0.53, and here we increase it up to 0.74 p.u., which immediately causes the measurements to change to different extent. Compared with other classifiers, our proposed method achieves the highest accuracy with less variations and hence is more robust to the load variations.

Also, we change the topology by varying the states of eight switches. Tables IV reveals the testing accuracy of the datasets with various switch states, where “Close 7&8” denotes that we close the switches 7 and 8 from open states, and “Open 1-6” means that we open the first 6 closed switches. Note that the challenge here is not only the change of topology, but also the data variations caused by topology changes. Still, the proposed one demonstrates better accuracy in all scenarios.

Table III: LAR of SPG, DPG, PP When All the Loads Vary in Different Ranges

	Δp (p.u.)	0.53	0.58	0.64	0.69	0.74
SPG	CNN	93.9	85.3	84	83.9	82
	NN	92.5	80	77.4	76.7	74
	GCN	64.3	57.7	56.4	55.6	55.1
	Proposed	98.9	96.6	96.3	95.8	95.1
DPG	CNN	96.5	88.3	87.8	85.3	82.5
	NN	98	89.3	88.2	86.7	85.1
	GCN	98.3	84.0	83.7	82.2	78.8
	Proposed	98.4	94.1	93.7	92.7	92.2
PP	CNN	97.5	96.2	96.1	95.1	94.6
	NN	95.6	92.2	90.3	87.9	85.9
	GCN	99.5	96.5	96.5	96.6	96.7
	Proposed	99.9	99.6	99.4	99.2	98.4

F. Effects of Various Adjacency Matrices

The choice of adjacency matrix of \mathcal{G}_1 impacts the location performance. We compare the performance of \mathcal{G}_1 when choosing different adjacency matrices in Fig. 7, where “Original” means the adjacency matrix is the admittance matrix from the original power grid, and “Proposed” denotes the adjacency matrix as defined by (4). We observe that \mathcal{G}_1 with A achieves better location accuracy rates at different label rates than that using admittance matrix. The advantages of A is the flexibility to deal with the low portion of measured nodes (around 16% in this test feeder) by tuning the k_1 .

Table IV: LAR of SPG When Different States of Switches Change Network Topology

	Switch	Close 7&8	Open 1-6	Open 1-3	Open 1&2
SPG	CNN	80.0	84.4	88.8	89.2
	NN	75.0	82.5	81.7	84.5
	GCN	56.9	58.3	59.6	62.2
	Proposed	95.8	94.5	96.9	97.9
DPG	CNN	84.7	88.3	90.3	92.5
	NN	82.9	91.0	89.3	93.7
	GCN	80.5	66.9	85.6	89.4
	Proposed	93.6	94.4	96.5	96.1
PP	CNN	96.1	95.0	96.9	96.8
	NN	93.6	94.1	94.1	95.2
	GCN	91.4	95.6	97.3	99.1
	Proposed	97.2	99.0	99.9	99.8

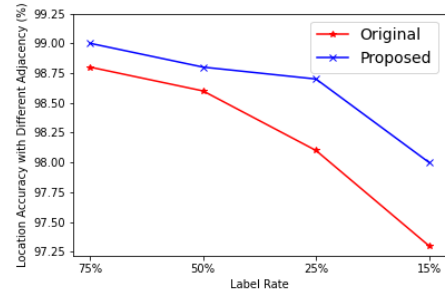


Fig. 7: Comparison of the location accuracy of all types of faults with Different Adjacency Matrices

G. Extension to IEEE 37-node Test Feeder and Advantages of the Proposed Training Strategy

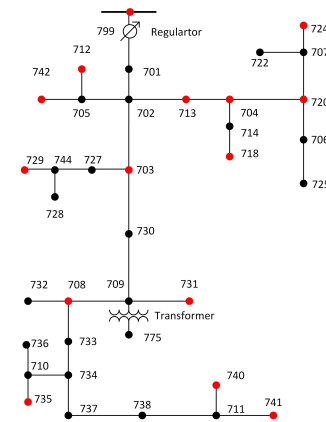


Fig. 8: The IEEE 37-bus test feeder [30]

Table V: Location Performance of All Types of Faults When Using Various Training Strategies

	β	75%	50%	25%	15%
Supervised Training	F1 Score	91.0	90.4	88.1	84.7
	LAR	91.1	90.3	88.2	84.8
	LAR ^{1-hop}	97.6	96.8	96.5	96.5
Proposed Training	β	75%	50%	25%	15%
	F1 Score	95.6	94.9	93.3	91.3
	LAR	95.6	94.9	93.3	91.3
LAR ^{1-hop}	98.9	98.5	99.1	98.9	

We extend our graph framework to the IEEE 37-node test feeder [30], as shown in Fig. 8, where the measured nodes are marked as red. To indicate the adaptation of our graph model, we keep the same graph structures described in Section V-A1. Only the dimensions of inputs become $\bar{X}^p \in R^{36 \times 6}$, $p \in [1, \bar{N}]$, $\bar{y}^p \in \{1, \dots, \bar{c}\}$, $\bar{c} = 36$, where \bar{X}^p only has 15 nonzero rows corresponding to those observed nodes. We generate $\bar{N} = 12960$ data samples in the 37-node test feeder, including SPG, PPG, and PP faults at all possible nodes, accompanied with load fluctuating. We train our graph framework with different percentages of datasets and test by the remaining data. The location performance of all types of faults is shown in Table V in the line of “Proposed Training”, which denotes that we employ the proposed training strategy in Section III-A4. Comparably, “Supervised Training” denotes that the graph model is trained by the conventional supervise learning method, i.e., regard \mathcal{G}_1 as a whole and update all the trainable parameters in Θ_1 in each iteration by optimizing (7).

Table V shows that the proposed training strategy can enhance up to 6% of LAR than that using “Supervised Training”. Note that the similar effectiveness also appears in the 123-node test feeder. The intuition behind is that the “local aggregation” and “global transformation”, functioning as the encoder and decoder of the graphical input data, have better convergence if trained alternatively [37, 48].

VI. CONCLUSIONS AND FUTURE WORKS

To enhance stable and resilient grid operation in the age of energy transformation, distribution grids need to efficiently and effectively respond to faulty conditions. Existing works on data-driven fault localization algorithms face practical challenges: low observation, insufficient labeled datasets, and dynamic data distributions. This paper presents a two-stage robust data-driven algorithm for fault location via embedding power grid physics into a graph learning framework.

The theoretical interpretations clarify the mechanism of constructing graph models to address the challenges of sparse observability and low label rates. Experimental results demonstrate superior performances of the proposed approach in locating faults over three baseline classifiers. A large number of ODD datasets validate our approach’s robustness to load variations and topology changes. In addition, our graph learning framework can smoothly be adapted to another distribution system and shows high performance with the proposed training strategy. Our future interest is to study the optimal deployment of μ PMUs to maximize location accuracy at the minimum cost.

REFERENCES

- [1] D. Novosel, G. Bartok, G. Henneberg, P. Mysore, D. Tziouvaras, and S. Ward, “IEEE PSRC report on performance of relaying during wide-area stressed conditions,” *IEEE Trans. Power Del.*, vol. 25, no. 1, pp. 3–16, 2009.
- [2] “U.S.—Canada power system outage task force: Final report on the implementation of task force recommendations,” [Online]. Available: <http://energy.gov/oe/downloads/us-canada-power-system-outage-task-force-final-report-implementation>, Jun. 2006.
- [3] “Smart grid system report,” United States Department of Energy, Washington, DC, USA, Accessed: Nov. 20, 2019. [Online]. Available: <https://www.energy.gov/sites/prod/files>, 2018.
- [4] “2019 Incident Archive,” <https://www.fire.ca.gov/incidents/2019>, 2019.
- [5] R. Dobbe, W. van Westering, S. Liu, D. Arnold, D. Callaway, and C. Tomlin, “Linear single- and three-phase voltage forecasting and bayesian state estimation with limited sensing,” *IEEE Trans. Power Syst.*, vol. 35, no. 3, pp. 1674–1683, 2020.
- [6] M. Majidi, M. Etezadi-Amoli, and M. S. Fadali, “A sparse-data-driven approach for fault location in transmission networks,” *IEEE Trans. Smart Grid*, vol. 8, no. 2, pp. 548–556, Nov. 2017.
- [7] M. Majidi, A. Arabali, and M. Etezadi-Amoli, “Fault location in distribution networks by compressive sensing,” *IEEE Trans. Power Del.*, vol. 30, no. 4, pp. 1761–1769, 2015.
- [8] J. Liu, C. Qin, and Y. Yu, “A comprehensive resilience-oriented flisr method for distribution systems,” *IEEE Trans. Smart Grid*, 2020.
- [9] S. M. Brahma, “Fault location in power distribution system with penetration of distributed generation,” *IEEE Trans. Power Del.*, vol. 26, no. 3, pp. 1545–1553, 2011.
- [10] I. Džafić, R. A. Jabr, S. Henselmeyer, and T. Đonlagić, “Fault location in distribution networks through graph marking,” *IEEE Trans. Smart Grid*, vol. 9, no. 2, pp. 1345–1353, 2016.
- [11] S. F. Alwash, V. K. Ramachandaramurthy, and N. Mithulananthan, “Fault-location scheme for power distribution system with distributed generation,” *IEEE Trans. Power Del.*, vol. 30, no. 3, pp. 1187–1195, 2014.
- [12] R. Dashti, M. Ghasemi, and M. Daisy, “Fault location in power distribution network with presence of distributed generation resources using impedance based method and applying π line model,” *Energy*, vol. 159, pp. 344–360, 2018.
- [13] S. Shi, B. Zhu, A. Lei, and X. Dong, “Fault location for radial distribution network via topology and reclosure-generating traveling waves,” *IEEE Trans. Smart Grid*, vol. 10, no. 6, pp. 6404–6413, 2019.
- [14] A. Phadke, “Synchronized phasor measurements in power systems,” *Computer*, 1993.
- [15] A. Von Meier, D. Culler, A. McEachern, and R. Arghandeh, “Micro-synchrophasors for distribution systems,” in *Innovative Smart Grid Technologies Conference (ISGT), 2014 IEEE PES*, 2014.
- [16] W. Li and D. Deka, “Physics informed neural network for high impedance faults detection,” in *2021 IEEE PowerTech Conference*.
- [17] Z. Lin, D. Duan, Q. Yang, X. Hong, X. Cheng, L. Yang, and S. Cui, “Data-driven fault localization in distribution systems with distributed energy resources,” *Energies*, vol. 13, no. 1, p. 275, 2020.
- [18] M. Majidi, M. Etezadi-Amoli, and M. S. Fadali, “A novel

- method for single and simultaneous fault location in distribution networks,” *IEEE Trans. Power Syst.*, vol. 30, no. 6, pp. 3368–3376, 2014.
- [19] H. Mirshekari, R. Dashti, A. Keshavarz, A. J. Torabi, and H. R. Shaker, “A novel fault location methodology for smart distribution networks,” *IEEE Trans. Smart Grid*, 2020.
- [20] K. Jia, B. Yang, X. Dong, T. Feng, T. Bi, and D. W. Thomas, “Sparse voltage measurement-based fault location using intelligent electronic devices,” *IEEE Trans. Smart Grid*, vol. 11, no. 1, pp. 48–60, 2019.
- [21] W. Li, D. Deka, M. Chertkov, and M. Wang, “Real-time faulted line localization and pmu placement in power systems through convolutional neural networks,” *IEEE Trans. Power Syst.*, vol. 34, no. 6, pp. 4640–4651, Nov. 2019.
- [22] K. Chen, J. Hu, Y. Zhang, Z. Yu, and J. He, “Fault location in power distribution systems via deep graph convolutional networks,” *IEEE Journal on Selected Areas in Communications*, vol. 38, no. 1, pp. 119–131, 2019.
- [23] Y. Yu, M. Li, T. Ji, and Q. Wu, “Fault location in distribution system using convolutional neural network based on domain transformation,” *CSEE Journal of Power and Energy Systems*, 2021.
- [24] D. Deka, S. Talukdar, M. Chertkov, and M. V. Salapaka, “Graphical models in meshed distribution grids: Topology estimation, change detection & limitations,” *IEEE Transactions on Smart Grid*, vol. 11, no. 5, pp. 4299–4310, 2020.
- [25] H. Hassani, R. Razavi-Far, M. Saif, and G.-A. Capolino, “Regression models with graph-regularization learning algorithms for accurate fault location in smart grids,” *IEEE Systems Journal*, 2020.
- [26] G. Cardoso, J. G. Rolim, and H. H. Zurn, “Application of neural-network modules to electric power system fault section estimation,” *IEEE Trans. Power Del.*, vol. 19, no. 3, pp. 1034–1041, June 2004.
- [27] W. Hamilton, Z. Ying, and J. Leskovec, “Inductive representation learning on large graphs,” in *Advances in neural information processing systems*, 2017, pp. 1024–1034.
- [28] T. N. Kipf and M. Welling, “Semi-supervised classification with graph convolutional networks,” *arXiv preprint arXiv:1609.02907*, 2016.
- [29] W. Hamilton, Z. Ying, and J. Leskovec, “Inductive representation learning on large graphs,” in *Advances in neural information processing systems*, 2017, pp. 1024–1034.
- [30] Distribution System Analysis Subcommittee, “IEEE 37 node test feeder,” [Online]. Available: <https://site.ieee.org/pes-testfeeders/resources/>.
- [31] W. H. Kersting, “Radial distribution test feeders,” *IEEE Trans. Power Syst.*, vol. 6, no. 3, pp. 975–985, 1991.
- [32] R. C. Dugan and T. E. McDermott, “An open source platform for collaborating on smart grid research,” in *2011 IEEE Power and Energy Society General Meeting*, 2011, pp. 1–7.
- [33] Q. Jiang, B. Wang, and X. Li, “An efficient PMU-based fault-location technique for multiterminal transmission lines,” *IEEE Trans. Power Del.*, vol. 29, no. 4, pp. 1675–1682, March 2014.
- [34] J. Calder, B. Cook, M. Thorpe, and D. Slepcev, “Poisson learning: Graph based semi-supervised learning at very low label rates,” in *International Conference on Machine Learning*. PMLR, 2020, pp. 1306–1316.
- [35] U. Von Luxburg, “A tutorial on spectral clustering,” *Statistics and computing*, vol. 17, no. 4, pp. 395–416, 2007.
- [36] Z. Yang, W. Cohen, and R. Salakhudinov, “Revisiting semi-supervised learning with graph embeddings,” in *International conference on machine learning*. PMLR, 2016, pp. 40–48.
- [37] I. Goodfellow, Y. Bengio, and A. Courville, *Deep Learning*. Cambridge, MA, USA: MIT Press, 2016.
- [38] M. Soltanolkotabi *et al.*, “Robust subspace clustering,” *Ann. Stat.*, vol. 42, no. 2, pp. 669–699, April 2014.
- [39] K. Xu, C. Li, Y. Tian, T. Sonobe, K.-i. Kawarabayashi, and S. Jegelka, “Representation learning on graphs with jumping knowledge networks,” in *International Conference on Machine Learning*, 2018, pp. 5453–5462.
- [40] P. W. Koh and P. Liang, “Understanding black-box predictions via influence functions,” in *International Conference on Machine Learning*. PMLR, 2017, pp. 1885–1894.
- [41] H. Wang and J. Leskovec, “Unifying graph convolutional neural networks and label propagation,” *arXiv preprint arXiv:2002.06755*, 2020.
- [42] A. Paszke and et al., “Pytorch: An imperative style, high-performance deep learning library,” in *Advances in Neural Information Processing Systems*. Curran Associates, Inc., 2019, pp. 8024–8035.
- [43] F. Pedregosa and et al., “Scikit-learn: Machine learning in Python,” *Journal of Machine Learning Research*, vol. 12, pp. 2825–2830, 2011.
- [44] F. Thabtah, S. Hammoud, F. Kamalov, and A. Gonsalves, “Data imbalance in classification: Experimental evaluation,” *Information Sciences*, vol. 513, pp. 429–441, 2020.
- [45] W. Li and M. Wang, “Identifying overlapping successive events using a shallow convolutional neural network,” *IEEE Trans. Power Syst.*, vol. 34, no. 6, pp. 4762–4772, Nov. 2019.
- [46] W. Li, M. Wang, and J. H. Chow, “Real-time event identification through low-dimensional subspace characterization of high-dimensional synchrophasor data,” *IEEE Trans. Power Syst.*, vol. 33, no. 5, pp. 4937–4947, Jan. 2018.
- [47] X. Zhu, Z. Ghahramani, and J. D. Lafferty, “Semi-supervised learning using gaussian fields and harmonic functions,” in *Proc. 20th Int. Conf. Machine learning (ICML-03)*, 2003, pp. 912–919.
- [48] W. L. Hamilton, R. Ying, and J. Leskovec, “Representation learning on graphs: Methods and applications,” *arXiv preprint arXiv:1709.05584*, 2017.